Continuum mechanics simulations of NiO/Ni–YSZ composites during reduction and re-oxidation

M.H. Pihlatie [a,b,*], H.L. Frandsen [a], A. Kaiser [a], M. Mogensen [a]

[a] *Risoe National Laboratory for Sustainable Energy, Technical University of Denmark, POB 49, DK-4000 Roskilde, Denmark*
[b] *VTT Technical Research Centre of Finland, POB 1000, FI-02044 VTT, Finland*

ARTICLE INFO

ABSTRACT

Repeated reduction–oxidation (redox) cycles on Ni-based solid oxide fuel cells (SOFC) have been experimentally well investigated and are known to be detrimental to the thermomechanical stability of the composites, especially on anode supported structures. In the present work the mechanistic analysis of the internal factors leading to the dimensional changes and the thermomechanical instability have been addressed, to our knowledge for the first time, using continuum mechanics simulations. The two intertwined percolating phases, YSZ and NiO/Ni, interact and the driving force for the dimensional change arises from the volumetric change related to the phase change NiO ↔ Ni. The measurable change in bulk length is given by the ceramic YSZ backbone as a response to the stress created by the chemical strain. The different subprocesses described in the model for YSZ were elastic and anelastic expansion, diffusional creep, grain boundary sliding (GBS) and microcracking due to excessive stress. In the Ni/NiO phase, nonelastic strains in terms of diffusional and power law creep were implemented, and additionally for NiO deformation due to microcracking and/or pseudoplasticity. Semi-empirical correlations were employed for creep limiting grain growth of Ni and NiO, particle coarsening of Ni and particle growth in NiO during the oxidation. Seven experimental cases of high temperature redox dilatometry were simulated. The model shows good qualitative agreement with the measurements. The different processes of importance for the dimensional behaviour are discussed.

© 2009 Elsevier B.V. All rights reserved.

1. Introduction

The SOFC commonly utilise Ni–YSZ microcomposites as anode materials. In the planar anode supported electrolyte (ASE) SOFC design these composites also serve as the structurally bearing support component for the cell. Both the anode support and the electrochemically active anode need sufficient porosity for gas transport and electrical conductivity, ensured by a percolating Ni-network. Typically 50–60 wt% of NiO is used in the ceramic manufacturing process. The second main component in the composite is an ionic conductor, often zirconia, in either fully or partially stabilised form by doping with secondary oxides of, e.g. yttrium. The anode substrate thus consists of three percolating intertwined phases: YSZ constitutes the stable ceramic backbone, metallic Ni gives the electrical, catalytic and electrochemical properties, whereas porosity ensures gas communication [1]. When the SOFC is taken into operation, the NiO contained in the anode structures is reduced at high temperature to Ni; this phase transformation

involves a volumetric shrinkage of 41% [2]. During high temperature operation at 600–1000 °C, the fine Ni particles are known to grow in size through a sintering process. The sintering can be facilitated by the presence of steam [3,4].

If metallic nickel is again exposed to an oxidising atmosphere at high temperature, the metal will readily oxidise; the phase change involves an expansion of 69% $\Delta V/V$. Further, if the existing porosity in the Ni–YSZ composite cannot accommodate this volume increase, large stresses are exerted by the expanding NiO phase on the ceramic backbone (and vice versa, by the rigid YSZ phase on the expanding Ni/NiO). As a direct proof of this force, a macroscopic expansion of the composite can be measured on isothermal re-oxidation. It has been verified that the magnitude of this redox strain is closely related to the operating conditions during both the initial reduction period and the re-oxidation [5], as well as the microstructure and composition of the composite itself [6]. The operating conditions affect the situation in two ways. First, sintering of Ni alters the cermet microstructure in an irreversible way, creating Ni grain growth and rearrangement. The growth of the Ni during re-oxidation cannot be fully accommodated by the existing porosity in the ceramic backbone. Secondly, during the re-oxidation process the temperature affects the thermomechanical response of the composite. The mechanism of Ni oxidation and the

* Corresponding author at: VTT Technical Research Centre of Finland, POB 1000, FI-02044 VTT, Finland. Tel.: +358 400 430395/45 1103464; fax: +358 20 7227048.
  E-mail addresses: mikko.pihlatie@vtt.fi, mikko.pihlatie@iki.fi (M.H. Pihlatie).

resulting microstructure, as well as the strength, elastic properties, creep, and stress relaxation of the materials depend on temperature. High temperature oxidation kinetics of Ni is known to be dominated by outward lattice diffusion of Ni at high temperatures. With decreasing temperature the contribution of short-circuit outwards diffusion along grain boundaries of Ni starts dominating. At still lower temperatures, the inwards diffusion of oxygen along grain boundaries and/or gaseous diffusion paths starts to play a role. Furthermore, grain growth and grain structure evolution of NiO in the temperature range 600–1000 °C are known to vary so that at the lowest temperatures, small equiaxed grains even close to the initial nucleation size can be retained, whereas at the highest temperatures rapid grain growth leading to columnar grains have been reported [7–10].

The durability and structural integrity of the SOFC depends, besides the mechanical stability of its components, on the geometrical design of the cell. A typical failure mode of the ASE cell is cracking of the electrolyte due to excessive tensile stress caused by expansions of the anode during re-oxidation. Mechanical modelling results suggest that such a cell can withstand about 0.1–0.2% $\Delta L/L$ strain on isothermal re-oxidation without cell failure [11–13]. Therefore, if dimensional stability at this level was achieved, it could enable a Ni-based SOFC tolerant to partial or even full re-oxidation. This paper attempts to further elaborate and discuss previous related experimental work [5,14] and the different internal processes taking place within the Ni–YSZ composite during the reduction–oxidation cycles. We have chosen an approach based on continuum mechanics to describe the dimensional response of a cermet to reduction and re-oxidation with different combinations of reduction and re-oxidation temperatures using both mechanistic and semi-empirical models. We aim to elucidate the thermomechanical processes of importance, starting from known chemical and physical processes and parameters, including measured reaction kinetics at different temperatures. In a modelling attempt of this kind, one soon finds that insufficient data exist on many areas, for example, the thermomechanical properties of partially oxidised Ni or partially reduced NiO grains, detailed grain structure information vs. temperature and time on Ni and NiO, and the stability and thermomechanical behaviour of interfaces; in such cases we have used known qualitative trends and best estimate approximations. Such semi-mechanistic approach can in the best case offer some possibilities for 'backwards' engineering where the relative importance of different processes can be interrogated by varying the loose or unknown parameters.

A continuum mechanics model was developed to describe the dimensional response of a NiO–YSZ composite to reduction and of the reduced cermet to subsequent re-oxidation. Seven redox dilatometry cases were run using a high precision dilatometer and are simulated using the model. The different processes of importance are discussed in light of the model simulations and available literature data.

2. Experimental

The study comprises microcomposites of NiO/Ni and yttria stabilised tetragonal zirconia polycrystals (Y-TZP) similar to those reported in earlier related studies [5,14]. Information on the ceramic processing of the samples as well as the experimental details regarding the dilatometry can be found in [5]. All dilatometry experiments were carried out in dry gas, using a Netzsch 402 CD differential dilatometer. Redox cycling was implemented by controlled sequences of air, N_2 and 9% H_2 diluted in N_2. All chemical phase change reactions were carried out in isothermal conditions; different combinations of reduction and re-oxidation temperature were tested as follows:

1. Reduction and re-oxidation at 600 °C.
2. Reduction and re-oxidation at 750 °C.
3. Reduction and re-oxidation at 850 °C.
4. Reduction and re-oxidation at 1000 °C.
5. Reduction at 1000 °C, re-oxidation at 850 °C.
6. Reduction at 1000 °C, re-oxidation at 750 °C.
7. Reduction at 1000 °C, re-oxidation at 600 °C.

In the results section these experimental cases shall be referred to by their Arabic numerals. Reduction–oxidation kinetics were determined for similar samples by thermogravimetic analysis (TGA) using a Netzsch STA 409 CD and identical temperature and gas change programmes compared with the dilatometer tests. Additional information on the TGA procedures can be found in [14].

3. The model

3.1. General

The model treats the porous NiO/Ni–YSZ composite as an isotropic continuum where the YSZ phase constitutes the stable ceramic backbone. Micron-sized NiO/Ni is embedded within the ceramic backbone as a percolating phase. The YSZ and NiO/Ni phases are connected to each other through a sub-micron-sized interface, which during high temperature exposure to reducing conditions will undergo changes due to surface energy minimisation in the nickel phase. This leads to the growth of Ni particles through sintering and to loss of interface length with YSZ (dewetting). We assume that the driving force for the observed dimensional changes in the composite is the known shrinkage of NiO upon reduction to Ni, and the expansion of Ni upon re-oxidation to NiO. The constraint by the YSZ backbone on the dimensional changes of the Ni/NiO phase will result in, in equilibrium, opposing stresses in the YSZ and Ni/NiO phases. The magnitude of the stresses exerted by the Ni/NiO phase on the ceramic backbone depend on the geometrical effects like porosity, interface length and wetting, as well as on different relaxation phenomena taking place in the composite. These relaxation processes give nonlinear contributions in the stress analysis and include plastic deformation (creep) of Ni, NiO and YSZ, but also cracking and relocation strain of either the NiO or the YSZ phase. The dimensional change of the composite is taken as the length change of the YSZ phase due to elastic, anelastic and plastic deformations (creep), and fracture. Elastic and anelastic deformations are reversible, whereas creep and cracking lead to permanent deformation of the substrate.

As discussed in the following, many physical phenomena interplay in a complex geometry of a two phase microstructure. In the present model the focus is on the material behaviour, and the microstructure has been simplified to a continuum, where stresses and deformations are related to one dimension. The basic structure of the model and the most important processes involved are illustrated in Fig. 1 for reduction of NiO–YSZ composites and in Fig. 2 for the re-oxidation of the Ni–YSZ cermet. In Fig. 1, the left side of the image corresponds to the YSZ backbone responding to the strains arising from the chemical reaction on the NiO/Ni side. The length change of the composite, also named the Cumulative Redox Strain (CRS), is the elastic plus nonelastic strain of the YSZ phase, where the nonelastic strain is the sum of different components,

$$\text{CRS} = \varepsilon_{YSZ} = \varepsilon_{e,YSZ} + \varepsilon_{Ne,YSZ}, \tag{1}$$

$$\varepsilon_{Ne,YSZ} = \varepsilon_{YSZ,ane} + \varepsilon_{YSZ,cre} + \varepsilon_{YSZ,cra}, \tag{2}$$

and $\varepsilon_{YSZ,ane}$ is the anelastic strain, $\varepsilon_{YSZ,cre}$ is creep, and $\varepsilon_{YSZ,cra}$ is strain due to microcracking of the YSZ. The nonelastic strain in the Ni phase, $\varepsilon_{Ne,Ni}$, arises in parts of operation where Ni is present. It is the sum of the relaxation from Ni creep, dewetting of the Ni–YSZ
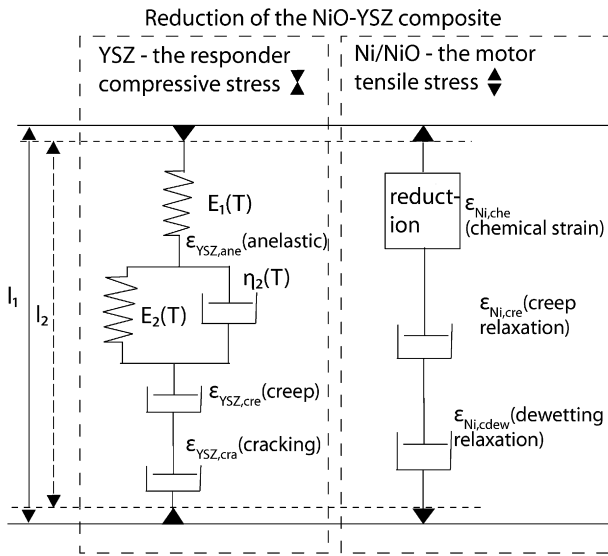
Fig. 1. The basic structure of the model during reduction, where the bulk length change of the composite is given by the elastic + nonelastic strain in the YSZ phase, and the stress state is generated by the chemical strain in the Ni/NiO phase.
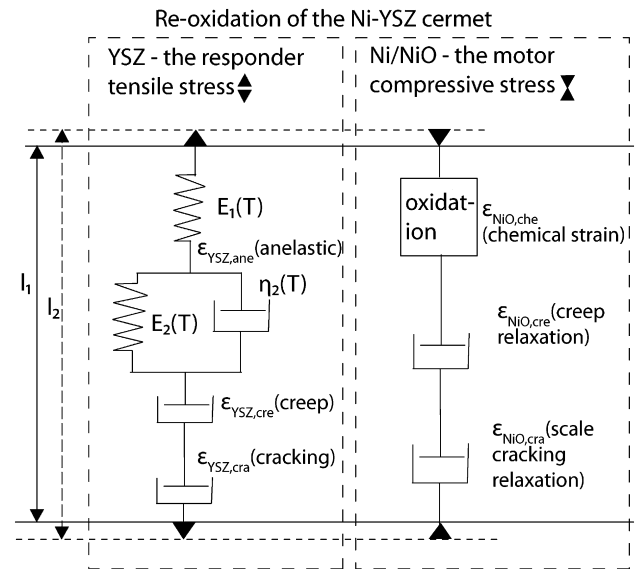

Fig. 2. The basic structure of the model during re-oxidation, where the bulk length change of the composite is given by the elastic + nonelastic strain in the YSZ phase, and the stress state is generated by the chemical strain in the Ni/NiO phase.

interface, and chemical strain

$$\varepsilon_{Ne,Ni} = \varepsilon_{Ni,cre} + \varepsilon_{Ni,dew} + \varepsilon_{red/ox,che}, \tag{3}$$

where $\varepsilon_{Ni,cre}$ is the creep strain of the Ni phase and $\varepsilon_{Ni,dew}$ is the effective relaxation of the chemical strain due to dewetting (a process closely related to the sintering of the Ni phase), and $\varepsilon_{red/ox,che}$ is the chemical strain. The Ni component is most active during the reduction process. During re-oxidation, the NiO phase shows nonelastic strain according to

$$\varepsilon_{Ne,NiO} = \varepsilon_{NiO,cre} + \varepsilon_{NiO,cra} + \varepsilon_{red/ox,che}, \tag{4}$$

where $\varepsilon_{NiO,cre}$ is the creep strain of the NiO phase and $\varepsilon_{NiO,cra}$ is the strain due to cracking and pseudoplasticity of the NiO phase.

The calculation proceeds as a time series simulation, where the chemical reaction kinetics in each case is taken from measured TGA data, and the chemical strains arise from those reactions. As

the specimens are not exerted external forces during the measurements, the total stress equals zero, and force equilibrium yields

$$\sigma(A_{Ni/NiO} + A_{YSZ}) = \sigma_{Ni/NiO}A_{Ni/NiO} + \sigma_{YSZ}A_{YSZ} = 0 \tag{5}$$

where A_i is the cross sectional area of the influenced part of the microstructure of phase i. Assuming that equal amounts of each of the phases are interacting through the interface (reasonable for similar stiffnesses and knowing the composition of the composite), Eq. (5) reduces to

$$\sigma_{Ni/NiO} = -\sigma_{YSZ}. \tag{6}$$

Hence, the stresses in the two phases are equal in magnitude but opposite in direction, and the different strains leading to this equilibrium are depicted in Fig. 3 during reduction and Fig. 4 during re-oxidation. The interaction through the interface also requires
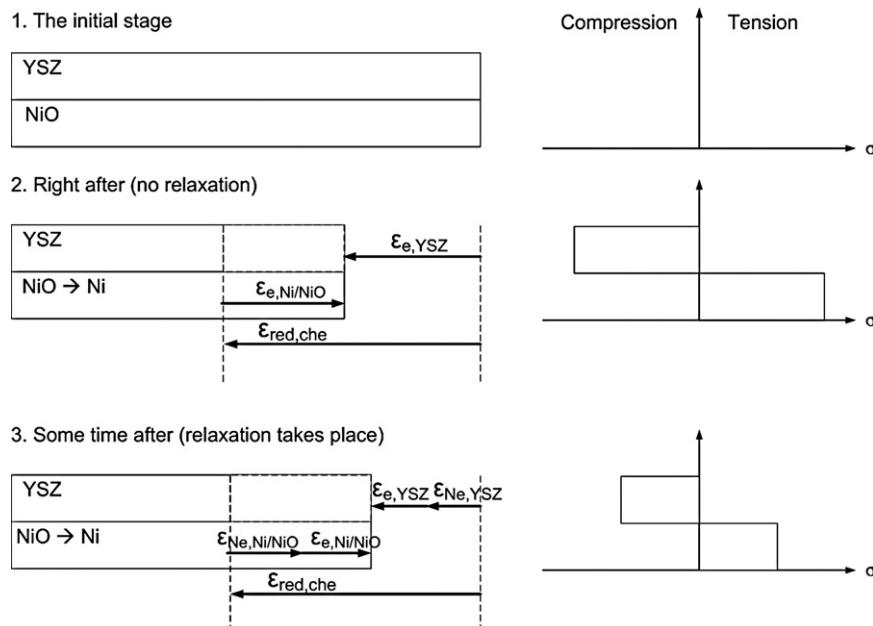

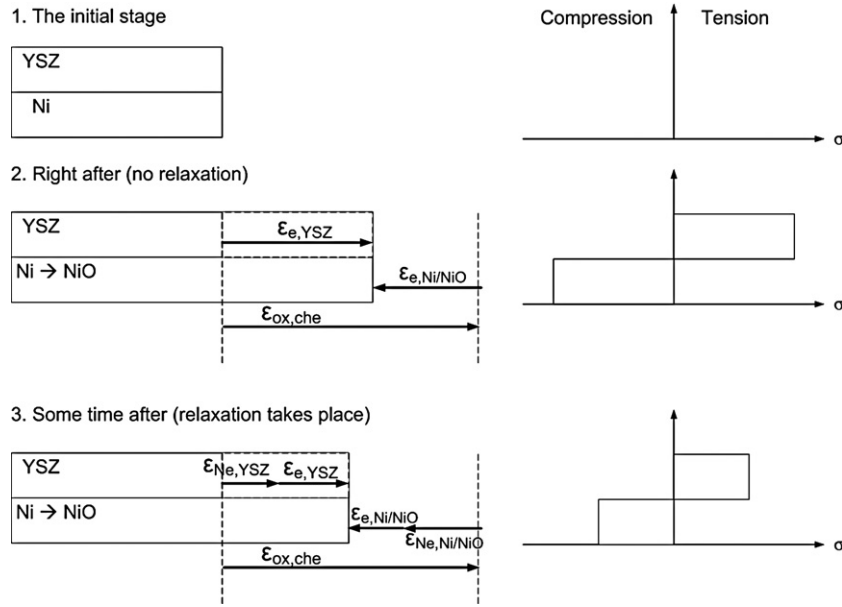**Fig. 3.** Strains and stresses during reduction of the NiO–YSZ composite.

Fig. 4. Strains and stresses during the re-oxidation of the Ni–YSZ cermet.

the total expansions, at the interface of the two different phases, to be equal

$$\varepsilon = \varepsilon_{Ni/NiO} = \varepsilon_{YSZ}, \tag{7}$$

where the total strain of the ith phase consists of the elastic strain and nonelastic strain of the phase

$$\varepsilon_i = \varepsilon_{e,i} + \varepsilon_{Ne,i}. \tag{8}$$

Assuming linear elastic material behaviour where the stress in the ith phase is proportional to the elastic strain in the phase

$$\sigma_i = E_i \cdot \varepsilon_{e,i}, \tag{9}$$

where E is the Young's modulus of the ith phase, and combining (6)–(9) provides

$$\sigma_{Ni/NiO} = E_{Ni/NiO}(\varepsilon - \varepsilon_{Ne,Ni/NiO}) = -\sigma_{YSZ} = -E_{YSZ}(\varepsilon - \varepsilon_{Ne,YSZ}), \tag{10}$$

which can be solved for the total expansion ε

$$\varepsilon = \frac{E_{Ni/NiO}\varepsilon_{Ne,Ni/NiO} + E_{YSZ}\varepsilon_{Ne,YSZ}}{E_{Ni/NiO} + E_{YSZ}} \tag{11}$$

such that the stresses can be obtained from Eq. (10).

In the numerical time discretisation the stresses in the present time step are calculated and knowing these the nonlinear strain contributions can be incremented to the following time step. The basic idea for the different mechanical property loss mechanisms, including sintering, dewetting and microcracking, is depicted in Fig. 5. The different physical and semi empirical submodels are

Table 1
Nomenclature and the values of the model parameters used in the simulations.

Parameter	Name	Value			Unit
		YSZ	NiO	Ni	
Anelastic spring 1	E_1	2 × Eq. (24)	2 × Eq. (23)	2 × Eq. (22)	Pa
Anelastic spring 2	E_2	2 × Eq. (24)	2 × Eq. (23)	2 × Eq. (22)	Pa
Anelastic viscosity, oxidised state	η_2	600 °C: 5E14; 750 °C: 1E14 850 °C: 8E13; 1000 °C: 6E13	–		
Anelastic viscosity, reduced state	η_2	600 °C: 5E14; 750 °C: 1E14 850 °C: 8E13; 1000 °C: 6E13	–		
Pre-exponential coefficient for diffusional creep	A_{diff}	9.3 [23]	98 × π [30]	42 [32]	–
Lattice diffusion coefficient	D_l	1.2 [27]	5E−3 [30]	1.9E−4 [32]	m² s⁻¹
Activation energy for D_l	Q	6.10E5 [27]	6 × 96320 [31]	2.84E5 [32]	J mol⁻¹
Grain boundary diffusion coefficient	D_{gb}	2.9E4 [27]	0.1 [30]	5E−5[a] [32]	m² s⁻¹
Activation energy for D_{gb}	Q	5.06E5 [27]	4 × 96320 [31]	1.15E5 [32]	J mol⁻¹
Shear modulus, room temperature	G_o	1.54E11 [23]	Eq. (23) × v[b]	7.89E10[c] [32,32]	Pa
Temperature coefficient for G	dG	3.52E7 [23]	–	−6.4E5[c] [32]	Pa K⁻¹
Burgers vector	b	2.57E−10 [23]	2.96E−10 [30]	2.49E−10 [32]	m
Atomic volume	Ω	–	1.83E−29 [30]	1.09E−29 [32]	m³
Stress exponent for diffusional creep	n	1	1	1	–
Grain size exponent for diffusional creep	p	3	3	2–3[d] [32]	–
Effective grain boundary thickness	δ	1E−9 [27]	7E−10 [30]	7E−10 [30]	m
Pre-exponential coefficient for power-law creep	A_{pow}	–	1E19 [30]	3E6 [32]	–
Stress exponent for power-law creep	n	–	8 [31]	4.6 [32]	–

[a] Calculated from [32] assuming the effective grain boundary thickness of 0.7 nm.
[b] Estimated using Eq. (23) and assuming a Poisson ratio of v = 0.3.
[c] The formula $G = G_o + (T − 300)/T_m \times dG$, T_m being the melting temperature, from [32] was used.
[d] The value of p is 2 for Nabarro-Herring creep and 3 for Coble creep.
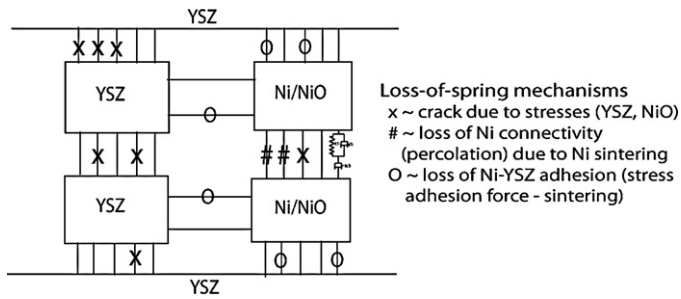
Fig. 5. A schematic presentation of the different mechanical loss processes taking place in the composite in the course of redox cycling.

discussed in the following.

3.2. Physical submodels

The values of all parameters discussed in this section and used in the model are listed in Table 1.

3.2.1. Chemical expansion

The chemical strain $\varepsilon_{Ni,che}$ arises due to the volumetric change from the reduction of NiO into Ni. The volumetric change upon reduction of NiO to Ni is 41%, resulting in a 16% linear strain. In the absence of any irreversible growth processes or microstructural change this chemical strain would be reversed on re-oxidation, that is, the particle size of the re-oxidised NiO would be identical to the initial as-sintered situation, with the chemical strain depending on the degree of oxidation (DoO),

$$\varepsilon_{red/ox,che} = DoO \cdot 0.16. \tag{12}$$

The value of DoO is one when the NiO is fully oxidised and zero when the reduction to Ni is complete. In reality, different irreversible processes take place so that the volumetric change on re-oxidation is larger than purely the volumetric change due to the chemical reaction. These processes include the sintering of Ni particles during operation, and the microstructural changes within the Ni/NiO phase during the oxidation.

The model takes into account the cermet total porosity increase upon reduction of the NiO into Ni. The 'effective' chemical volume expansion creates a stress on the YSZ phase on re-oxidation when the size of the oxidising NiO grain is larger than the original NiO particle size. This is in a simplified way taken care of using a semi-empirical temperature dependent parameter for Ni particle growth during operation under reducing conditions, and another parameter for the growth of the NiO particles during the re-oxidation. On reduction, the chemical strain becomes 'effective' when $DoO < 0.9$.

3.2.2. Anelastic expansion

The reversible anelastic strain (or primary creep), arises from the standard anelastic solid composed of a series connection of the Hookean spring with Young's modulus E_1, and the parallel connection of the spring E_2 and dashpot with viscosity η_2. The time dependent strain of this system is given by

$$\varepsilon_{YSZ,ane} = \varepsilon_1 + \varepsilon_2 = \frac{\sigma}{E_1} + \frac{\sigma}{E_2}\left(1 - \exp\left(-\frac{E_2}{\eta_2} \cdot t\right)\right). \tag{13}$$

Anelasticity results in a delayed strain response to stress, depending on the viscosity η under the given conditions. This type of behaviour is well known in crystalline solids [15,16] and has been reported to be significant in tetragonal zirconia polycrystals (TZP) [17–20]. Due to the high temperatures, however, the viscosity parameter can be expected to be quite high.

3.2.3. Creep

The creep of ceramics including the different flow mechanisms have been reviewed in many textbooks and papers, for example, [21–23]. The main mechanisms for creep deformation can be grouped according to the normalised stress σ/G, G being the shear modulus, as follows [21]:

- Dislocation glide, involving dislocations moving along slip planes. Active at high stress with $\sigma/G > 10^{-2}$.
- Dislocation creep, involving the movement of dislocations, which overcome barriers by thermally assisted mechanisms involving the diffusion of vacancies or interstitials. Occurs within $10^{-4} < \sigma/G < 10^{-2}$.
- Diffusion creep, involving the flow of vacancies and interstitials through a crystal under the influence of an applied stress. Occurs within $\sigma/G < 10^{-4}$.
- Grain boundary sliding (GBS), involving the sliding of grains past each other [24].

Generally, the steady state diffusion creep rate may be expressed in the form

$$\dot{\varepsilon} = \frac{ADGb}{kT}\left(\frac{b}{d}\right)^p\left(\frac{\sigma}{G}\right)^n, \tag{14}$$

where D is the appropriate diffusion coefficient, b is the Burgers vector, k is Bolzmann's constant, T the absolute temperature, d the grain size, σ the applied stress, and n and p the stress and the inverse grain size exponent, respectively. Both the diffusion coefficient and the shear modulus depend on temperature,

$$D = D_o \exp\left(\frac{-Q}{RT}\right), \tag{15}$$

where Q is the activation energy and R the gas constant, and

$$G = G_o - dG \cdot T, \tag{16}$$

where dG is the temperature dependency coefficient for G and T in K. If n is close to unity, the creep rate is close to linear dependence with the stress and the creep mechanism is based on diffusional flow. Then, the creep rate is controlled by the slowest diffusing species. Further, if the diffusion takes place through the bulk of the material, it is commonly called Nabarro-Herring creep [25] with $p = 2$ and $n = 1$ in (14) giving the grain size and stress dependencies. If instead grain boundary diffusion is dominant, the deformation mechanism is termed Coble creep [26]; then in (14) $p = 3$ and $n = 1$. In practice, the Coble and Nabarro-Herring creep act independently in parallel. Power-law creep is independent of grain size so that $p = 0$, and the value of the stress exponent n can vary from material to material, typically in the range from 3 to 8 [21,23].

For YSZ, a diffusion creep law combining the two mechanisms was implemented according to [23]

$$\dot{\varepsilon} = A_{diff}\frac{D_l Gb}{kT}\left(\frac{b}{d}\right)^2\left(\frac{\sigma}{G}\right)\left[1 + 3.6\frac{D_{gb}}{D_l}\left(\frac{\delta}{d}\right)\right], \tag{17}$$

where D_{gb} is the diffusion coefficient for grain boundary diffusion and D_l for lattice diffusion of the rate-limiting species. The creep limiting cation diffusion coefficients in tetragonal zirconia were taken from Chokshi [27], and shown in Table 1. The diffusional creep deformation was reported by Chokshi to be dominated by Coble creep. What is more, the diffusivities in cubic and tetragonal zirconia were relatively close to each other, however, grain growth in TZP is suppressed by Y segregation at grain boundaries [27].

GBS is known to play an increasingly significant role in zirconia at elevated temperatures and stresses [24]. At high temperatures above 1000 °C, GBS leads to superplasticity; under superplastic conditions remarkable plastic deformations can be achieved without brittle failure. GBS in zirconia has been suggested to be associated

with a critical onset stress σ_o, depending on the temperature and the grain size d,

$$\sigma_o = \frac{3 \times 10^{-4}}{d} \exp\left(\frac{1.2 eV}{kT}\right), \tag{18}$$

where σ_o is expressed in MPa and d in μm. The strain rate due to GBS becomes, using (18), [28,29]

$$\dot{\varepsilon} = 3 \times 10^{10} \frac{(\sigma - \sigma_o)^2}{Td^2} \exp\left(-\frac{4.7\,eV}{kT}\right), \tag{19}$$

where again σ_o is expressed in MPa and d in μm. In the present model, the creep deformation of YSZ was implemented as a sum of creep components from diffusional flow (17) and GBS (19),

$$\varepsilon_{YSZ,cre} = \varepsilon_{YSZ,diff} + \varepsilon_{YSZ,gbs}. \tag{20}$$

This formulation of the YSZ creep will effectively lead to linear diffusional creep flow at moderate temperatures and stresses, and an amplified deformation due to GBS at elevated temperatures or high stresses, depending on the microstructure.

The creep of NiO for both single crystals and polycrystals has been studied in the literature. Jiménez-Melendo et al. have reported creep experiments of NiO polycrystals, including deformation maps [30,31]. The creep of NiO polycrystals was described as Coble creep $\varepsilon_{NiO,gb}$ at low stresses, and additionally power law creep $\varepsilon_{NiO,pow}$ at higher stresses (σ larger than about 30 MPa). The conditions for Nabarro-Herring creep (bulk diffusion) could not be reached in their experiments. The creep of the NiO phase is given by the sum of the two,

$$\varepsilon_{NiO,cre} = \varepsilon_{NiO,pow} + \varepsilon_{NiO,gb}, \tag{21}$$

with the creep rates from [30,31],

$$\dot{\varepsilon}_{NiO,pow} = A_{pow} \frac{Gb}{kT} \left(\frac{\sigma}{G}\right)^n D_o^l, \tag{22}$$

and

$$\dot{\varepsilon}_{NiO,gb} = A_{diff} \frac{\sigma\Omega}{kTd^3} \delta D_o^{gb}. \tag{23}$$

In (22 and 23), A_{pow} and A_{diff} are constants, Ω the atomic volume of NiO, δ the effective grain boundary thickness and D_o^l and D_o^{gb} the diffusion coefficients for lattice and grain boundary diffusion, respectively. The values of the parameters are given in Table 1.

For metallic Ni, the creep formulations were taken from [32]. The deformation mechanism maps are a practical tool in evaluating the type and rate of deformation under different conditions. For metallic nickel with melting temperature $T_m = 1726$ K, the homologous temperatures (T/T_m) relevant in this work are in the order of 0.3–0.6. Generally, the high temperature creep can be divided into two regions. At low stress levels, diffusional creep takes place. Within the diffusional creep, at lower temperatures the dominating mechanism is grain boundary diffusion and at high temperatures lattice diffusion. Secondly, at higher stress levels the steady state creep rate follows the general power law where the creep rate is proportional to

$$\dot{\varepsilon} \propto \left(\frac{\sigma}{G}\right)^n, \tag{24}$$

where the stress exponent n can vary from 3 to 10 [32]. The creep mechanism depends on the mobility of dislocations. Within the power law domain, at high temperatures and low stresses, lattice diffusion is dominant. At lower temperatures, or higher stresses, core diffusion becomes dominant, and the strain rate varies according to $n+2$ [32]. For Ni creep, the following rate equations were implemented. For diffusional flow, the creep rate is given by [32]

$$\dot{\varepsilon}_{Ni,diff} = \frac{42\sigma\Omega}{kTd^2} D_{eff}, \tag{25}$$

with the effective diffusion coefficient D_{eff} defined as

$$D_{eff} = D_l \left[1 + \frac{\pi\delta}{d}\frac{D_{gb}}{D_l}\right]. \tag{26}$$

The combination of Eqs. (25) and (26) leads to a steady state creep rate calculation where grain boundary diffusion controls the deformation at lower temperatures and lattice diffusion takes over at higher temperatures. In the power-law creep domain, the rate equation for the steady state creep is [32]

$$\dot{\varepsilon}_{Ni,powe} = \frac{AD_{eff}Gb}{kT}\left(\frac{\sigma}{G}\right)^n, \tag{27}$$

where A is a constant and the effective diffusion coefficient is in this case

$$D_{eff} = D_l \left[1 + \frac{10a_c}{b^2}\left(\frac{\sigma}{G}\right)^2\frac{D_c}{D_l}\right]. \tag{28}$$

In (28), a_c is the cross-sectional area of the dislocation core ($a_c \approx 2\delta^2$) and D_c the core diffusion coefficient. The two Eqs. (27) and (28) effectively lead to two combined power law equations, with lattice diffusion dominating at high temperatures and core diffusion at lower temperatures. Finally, the total Ni creep is in the model given by the sum of the diffusional (25) and the power-law (27) rate equations as

$$\varepsilon_{Ni,cre} = \varepsilon_{Ni,diff} + \varepsilon_{Ni,pow}. \tag{29}$$

3.2.4. Mechanical material parameters

The key mechanical parameters were taken from literature. The dependency of Young's modulus of NiO/Ni–YSZ composites on temperature and porosity was discussed in [33]; the dependency of Young's modulus on porosity is largely linear in a large porosity range for both NiO–YSZ and Ni–YSZ. While the Young's moduli at room temperature of NiO, Ni and YSZ are relatively close to each other, the temperature dependencies show some differences. For NiO, the correlation used was according to Menzies and Strafford [34] and taken as a linear fit to the average of their data given for pure and industrial grade oxidised Ni,

$$E_{NiO} = -0.3287 \cdot T + 437.7, \tag{30}$$

with E given in GPa and T in °C and the relevant range for application is taken as 600–1000 °C. At lower temperatures NiO has the characteristic peak around the Néel temperature of 250 °C, followed by linear decrease above that [33]. For Ni, the data from Farraro and McLellan [35] was used, giving

$$E_{Ni} = -9.33 \times 10^{-2} \cdot T + 242 \tag{31}$$

in the temperature range 400–1000 °C. For YSZ, Atkinson and Selcuk [36] have reported Young's modulus (GPa) from room temperature to 800 °C [36] as

$$E_{YSZ} = -0.0426 \cdot T + 191.06. \tag{32}$$

Linear extrapolation of (32) up to 1000 °C was implemented in the model.

3.2.5. Relaxation and expansions from cracking

Relaxation by cracking of the ceramic phase (YSZ and NiO) is possible above certain critical stress levels; in these cases the simulated stress in the composite does not exceed the critical fracture strength, but instead relaxation strain due to cracking is produced equal to the magnitude of the chemical strain during that time step. In the model, relaxation due to cracking can occur both in the YSZ and the NiO phase. The measurable length change of the composite is taken as $\varepsilon_{Ne,YSZ}$. Another approach, which was however not

used in the present work, would have been to implement a strain-dependent damage variable causing loss in the Young's modulus, e.g., as defined for the composite in [33].

The Weibull strength of NiO–YSZ composites in ball-on-ring tests for disk samples of 20 mm diameter and strip samples in uniaxial tension tests have been determined to be in the order of σ_o = 300 MPa [37] (with an efficient volume 0.5 mm^3). In ceramics, the strength and fracture failures are usually dealt with Weibull statistics. The rupture strength of 3Y-TZP samples was determined in [38], giving a quite linearly decreasing rupture strength for the tetragonal zirconia as a function of temperature. In the calculation of failure probability, the sample volume plays a role through the scaling law, valid for sample populations obeying the Weibull distribution [39]

$$\sigma_2 = \sqrt[m]{\frac{V_1}{V_2}} \cdot \sigma_1. \tag{33}$$

In a typical SOFC microcomposite the characteristic microstructural length scale is roughly 1–1.5 μm. Upon re-oxidation of the Ni the expansion exerts large local stresses on the ceramic structure and creates damage, as discussed by Klemensø [40]. This internal damage is first microscopic, leading to increasing redox strain, and becomes macroscopic through crack propagation. The porous composite could be viewed as a complex three-dimensional structure composed of a large number of Hookean springs or anelastic spring-dashpot elements connected in series and in parallel combined to produce the bulk properties. The primary response to the chemically induced stresses arises, however, at the microscopic level close to the interface between the NiO/Ni and YSZ. This suggests that the 'local' strength to microscopic failure can be estimated using the scaling law and the strength determined for macroscopic samples. Doing this rough calculation for rupture strengths measured for the composites at room temperature [37], the estimated strength for a 1 μm^3 efficient volume at room temperature becomes about 840 MPa (m = 20). The strength of ceramics varies with temperature. This is especially true for partially stabilised zirconia where the transformation hardening through crack tip passivation due to the martensitic tetragonal–monoclinic transformation becomes thermodynamically less favoured with increasing temperature. Although literature data on this aspect is scarce, it can be expected that the strength of TZP at 600 °C is somewhat higher than at 850 or 1000 °C. Based on (33), m = 20, the efficient volumes V_1 = 0.5 mm^3 and V_2 = 1 μm^3, and the information from [38], the following rupture strength values are obtained for V_2: 1497, 1198, 1089 and 681 MPa at temperatures 600, 750, 850 and 1000 °C, respectively. Danzer discusses that for samples with very small volumes the strength may be overestimated by the Weibull approach due to flaw size vs. efficient volume effects, in other words, the very small samples do not follow Weibull statistics [41]. We have used the strength of TZP at the micrometric scale (V_2) as a fitted parameter in the calculations. The results shown in the following section were obtained by using 710–780 (the lower value for case 7, the higher one for case 1), 540-570 (the lower value for case 6, the higher one for case 2), 390–410 (the lower value for case 5, the higher one for case 3) and 210 (case 4) MPa for the rupture strength of the YSZ phase for local microscopic cracking and for the re-oxidation temperatures of 600, 750, 850 and 1000 °C, respectively.

The mechanical behaviour of the NiO scales during oxidation has been discussed in [42,43]. In isothermal oxidation the stresses are generated by the volumetric change, characterised by the Pilling–Bedworth ratio for Ni of 1.65 [7]. The exact thermomechanical behaviour during the oxidation depends on the oxidation mechanism. The stresses in the oxide scales can be relieved either by plastic deformation (creep) or by crack formation. In the porous composite these relaxation processes can occur in both the YSZ and

the Ni/NiO phase. The NiO phase is expanding into existing porosity within the ceramic backbone; therefore if this free expansion volume is used up, a tensile force (and subsequent bulk redox strain) arises, combined with a simultaneous similar compressive force on the NiO phase; this is equal to our earlier discussion on the *effective* chemical strain. The NiO phase thus experiences two different compressive forces during oxidation: one 'internal' stress from the scale development and another 'external' one from the geometrical constraints induced by the YSZ. For stress relaxation by creep in the NiO phase, correlations were given above. An additional mechanism, stress relaxation by scale cracking, pseudoplasticity and crack healing has been discussed by Küppenbender and Schütze [42,43].

Stress relaxation in the NiO phase takes place by creep until a critical strain ε_{crit}, where microcracking of the oxide is initiated. This strain depends on the fracture toughness of the oxide, K_{IC}, the Young's modulus and a geometrical factor f with a value of close to unity [42]

$$\varepsilon_{crit} = \frac{K_{IC}}{f E_{NiO} \sqrt{\pi c}}, \tag{34}$$

where c is the size of the most critical physical defect, such as a crack, microcrack or a void in the oxide. By utilising the Young's modulus of the material, the corresponding critical stress can be calculated as

$$\sigma_{crit} = E_{NiO}\varepsilon_{crit}. \tag{35}$$

The procedure to estimate the critical defect size c in (34) was discussed in [44]. The value of c depends on the type of defects, for instance, surface or embedded defects. For embedded defects the value of c used is the half width of the embedded defect, for through scale defects the value of c represents the half length of the crack [44]. In the absence of detailed microstructural analysis of the present composite on re-oxidation, an approximate value

$$c = DoO \cdot p_{NiO} \tag{36}$$

was used, where p_{NiO} is the (average) NiO particle size. Another aspect related to the thermomechanical behaviour of the NiO scales is the effect from microstructure and porosity. As shown by Radovic and Lara-Curzio [45] regarding macroscopic behaviour, the fracture toughness decreases with porosity, at least by a factor of about 2 when going from fully dense materials to porosities relevant for the current composites. The fracture toughness of NiO based on acoustic emission measurements has been reported by Bruns and Schütze to be in the range of 2–6 MPa $\sqrt{m}$ at 800 °C [46]. Furthermore, measurements in the brittle region at room temperature showed a considerably lower K_{IC} of 0.28–0.43 MPa $\sqrt{m}$ if the cracks were initiated at pores within the scale, and 0.74–1.3 MPa $\sqrt{m}$ if microcracks acted as crack starters. Evans et al. also conclude [47] that the strength decreases rapidly with porosity in the brittle region, however, for NiO the brittle-to-ductile transition starts already at about 600 °C where the effect from porosity on fracture stress is not as strong as at room temperature. How much ductility is present in the oxide scale depends additionally on the grain and pore sizes in the NiO. The value of K_{IC} = 1.5 MPa $\sqrt{m}$ was used in the model.

Küppenbender and Schütze further discuss the dynamic behaviour of the scales during oxidation [42,43]. The microcracks can either dynamically heal, leading to pseudoplasticity, or develop into permanent micro and macrocracks with direct gaseous diffusion path to the metal interface. Whether or not the healing process and pseudoplasticity can take place can be assessed by [42,43]

$$\dot{\varepsilon}_0^H = \frac{2k_p}{l_R d}, \tag{37}$$

where $\dot{\varepsilon}_0^H$ is the maximum tensile strain rate at which instant healing the microcracks is possible, k_p is the parabolic rate constant of oxidation, l_R the distance between microcracks and d is the scale

Table 2
Empirical coefficients used to calculate the pre-logarithmic parameter for the particle and grain size of Ni and NiO as a function of time from the chemical phase change. For NiO the particle size describes the effective particle size including the closed or open porosity developing in the particle due to the oxidation process. Note that T is given in °C. Parameters are well defined within the temperature interval 600–1000 °C.

	Coefficient for T^2	Coefficient for T^1	Coefficient for T^0
Ni particle size p_{Ni} (a)	2.00E−7	−1.82E−4	0.041
Ni grain size d_{Ni} (b)	3.07E−6	−2.63E−3	0.562
NiO effective particle size p_{NiO} (e)	9.17E−7	−3.56E−4	−0.051
NiO grain size d_{NiO} (c)	2.00E−5	−2.00E−2	5.00

thickness. If in this assessment the circumferential compressive strain rate is less than the maximum strain rate $\dot{\varepsilon}_0^H$, pseudoplasticity can occur and can NiO deform to relieve the re-oxidation stress without cracking. In the present calculation it is assumed that when the calculated stress at a time step exceeds the calculated critical stress for NiO microcracking, given by Eq. (35), the NiO phase deforms (either with or without dynamic healing) to relieve the effective chemical (oxidation) strain as it is generated.

3.3. Semi-empirical correlations

The mechanisms causing SOFC degradation have recently been reviewed by Yokokawa et al. [48]. One of the main degradation mechanisms on the Ni–YSZ anodes is the growth of Ni grains due to sintering and other transport processes, and the related degradation of the electrical and electrochemical properties. Fine nickel grains are known to grow in size in both microcomposites of Ni–YSZ [3] and in fine particle nanocatalysis [4,49]. The minimisation of the surface energy in Ni leads to changes in the surface morphology. Also, the Ni grains grow in size due to lattice and surface diffusion, and possibly also the gas phase through evaporation–condensation; these different mechanisms are generally referred to as sintering in the present paper. Both solid state diffusion and gaseous volatility are driven by temperature. The sintering is amplified by humidity through the increased gas pressure and the mobility of the Ni_2–OH formed, as pointed out by Sehested et al. [49]. The formation of the hydroxide is favoured by high $p(H_2O)/p(H_2)$ ratio in the gas. The implications of Ni grain growth for redox stability were discussed in [50]. Electrical conductivity is a good in situ measure to monitor and quantify the microstructural changes in the cermet; sintering of Ni leads to the loss of percolation and degrades the electrical conductivity of the cermet. The conductivity degradation is initially fast and slows down to finally reach a plateau characteristic of the cermet microstructure and the operating conditions. This type of behaviour is qualitatively shown in [40,51]; based on these and some to date unpublished data by the present authors, a phenomenological correlation for Ni particle size p_{Ni} was implemented in the model as follows. The particle size of Ni is given by

$$p_{Ni}(t) = p_{o,Ni}(1 + a \cdot \log(t)), \tag{38}$$

where $p_{o,Ni}$ is the initial particle size, time is in s, and a is an empirical pre-logarithmic parameter depending on T defined as

$$a = a_2 \cdot T^2 + a_1 \cdot T + a_0, \tag{39}$$

where T is given in °C and the parameters a_i in Table 2.

In the simulations, the creep deformation of the Ni phase comes mainly through the power-law correlation (27). For the diffusional creep component in Ni, grain size d plays some role, as shown in (25). In the absence of relevant grain growth data on Ni it was modelled as

$$d_{Ni}(t) = d_{o,Ni}(1 + b \cdot \log(t)), \tag{40}$$

where b is defined as in (39), and the parameters b_i given in Table 2. Here d_{Ni} is considered to be the creep rate determining

grain/subgrain structure and a substructure of p_{Ni}. If d_{Ni} becomes larger than p_{Ni} in the calculation, then the value of p_{Ni} is used.

The oxidation mechanism plays a role for the microstructural evolution of the NiO phase. At high temperatures of around 1000 °C or above the rate determining oxidation mechanism is outward diffusion of Ni, whereas at lower temperatures an increasing contribution arises from the outward grain boundary diffusion of Ni and inward short circuit diffusion of O. The inward diffusion of oxygen can, besides grain boundary diffusion, also take place along porosity, cracks or micro fissures in the oxide [7–9]. The grain size of NiO resulting from the re-oxidation of Ni within the composite depends on the primary recrystallisation and grain growth with time. Grain size has been treated in the literature to follow a parabolic to the 4th power dependency with time, and additionally approach a rather constant value after long exposure [52]. Atkinson investigated the grain structure evolution of NiO scales and found that the grain structure is initially very fine, of submicron size, and undergoes rapid grain growth at high temperatures [10]. In the present simulations the creep rate limiting NiO grain size plays a role through Eq. (23). The time dependency of NiO grain growth was modelled using the logarithmic form

$$d_{NiO}(t) = d_{o,NiO}(1 + c \cdot \log(t)), \tag{41}$$

with the parameter c defined as in (39) and coefficients c_i given in Table 2. Again, the creep rate controlling grain/subgrain size d_{NiO} is a substructure of the NiO particle. The grain size values obtained using the simple correlation (41) are in fair neighbourhood of the rate controlling grain sizes reported by Haugsrud of about 0.6, 1, 2 and 8 µm for temperatures 600, 750, 850 and 1000 °C, respectively [9].

For the NiO particle size we used the similar form of correlation, now with

$$p_{NiO}(t) = p_{o,NiO}(1 + e \cdot \log(t)), \tag{42}$$

with the coefficients e_i again given in Table 2. The particle size of NiO is taken as the effective particle size, including the porosity that is known to develop within the NiO phase. After low temperature re-oxidation the NiO phase is fine structured and contains fine closed porosity, whereas high temperature re-oxidation leads to larger NiO grains where also the pore size is considerably larger [5]. In another investigation [6] on Ni–ScYSZ re-oxidised and subsequently reduced anodes we saw that the Ni was smeared out against the ceramic cavity walls. After low redox cycling at 650 °C the Ni microstructure as well as the pore size was clearly finer than after redox cycling at 850 °C, furthermore, redox cycling at the latter temperature created visible cracking in the ceramic backbone due to excessive stress build-up.

The creep properties of partially reduced NiO and partially oxidised Ni are not fully known. From the existing creep formulations on Ni and NiO it is easy to conclude that under similar conditions, the creep rate of Ni is clearly higher than that of NiO. It has also been verified for Ni–YSZ microcomposites with the Ni content around the percolation threshold (∼40 vol% Ni) that the Ni–YSZ shows a more ductile behaviour and higher creep rates than oxidised NiO–YSZ composites [53,54]. In a reducing NiO grain the chemical reaction proceeds from the outer shell of the grain into the

Table 3
Empirical parameters used in defining the effective degree of oxidation for relaxation strain components form the Ni and NiO phases in partially reduced/oxidised Ni/NiO grains.

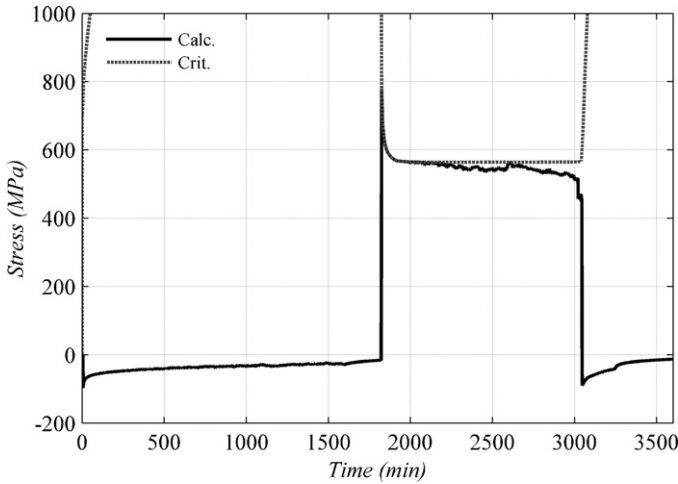|	n	m
Reduction (n_{red}, m_{red})	1	5
Oxidation (n_{ox}, m_{ox})	1.8	0.125

Fig. 6. Case 1: Calculated stress and the critical stress for NiO fracture during isothermal reduction and re-oxidation at 600 °C.

interior. The Ni phase more readily responds to the tensile stress originating from the chemical reaction. Furthermore, during the course of the reduction, the ability of the diminishing NiO core to deform as a response to the stress vanishes and the creep of the mixed Ni/NiO phase is dominated by Ni creep. This was taken into account in the model by defining an empirical *effective $DoO_{eff,red}$* for creep relaxation during reduction as

$$DoO_{eff,red} = (n_{red} \cdot DoO)^{m_{red}}, \tag{43}$$

where the parameters n_{red} and m_{red} are given in Table 3. In a similar manner, during the oxidation phase the growing oxide scale develops on the surface of the Ni grains and we claim that the growing NiO shell will rapidly start controlling the creep rate of the Ni/NiO phase. Again, an empirical *effective $DoO_{eff,ox}$* pertaining to the re-oxidation phase was defined according to

$$DoO_{eff,ox} = (n_{ox} \cdot DoO)^{m_{ox}}, \tag{44}$$

with n_{ox} and m_{ox} given in Table 3.

4. Results

Results obtained from the simulations of the dimensional behaviour of typical Ni–YSZ composites during redox cycling are presented for each case in the following. For case 1 (reduction and re-oxidation at 600 °C), the calculated stress and the critical stress for NiO microcracking are shown in Fig. 6. Fig. 7 shows the measured CRS in dilatometry and the CRS (elastic + nonelastic strain in the YSZ) calculated by the model as a function of time. The different deformation mechanisms leading to stress relaxation are shown Fig. 8. The similar graphs are given in Figs. 9–11 for case 2 (reduction and re-oxidation at 750 °C), Figs. 12–14 for case 3 (reduction and re-oxidation at 850 °C), Figs. 15–17 for case 4 (reduction and re-oxidation at 1000 °C), Figs. 18–20 for case 5 (reduction at 1000 and re-oxidation at 850 °C), Figs. 21–23 for case 6 (reduction at 1000 and re-oxidation at 750 °C), and Figs. 24–26 for case 7 (reduction at 1000 and re-oxidation at 600 °C), respectively.
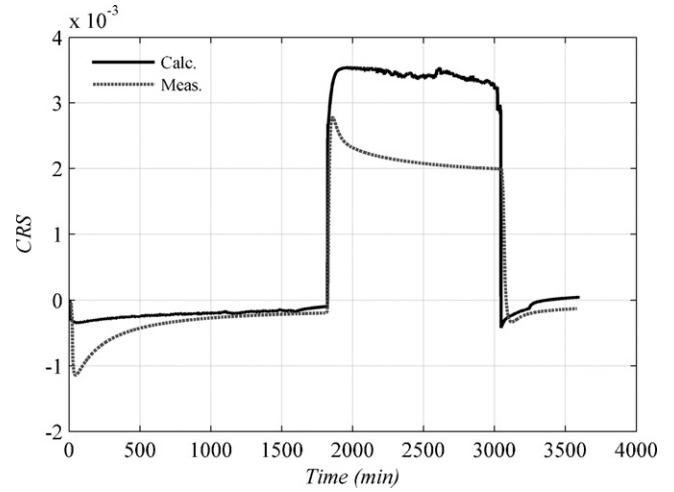
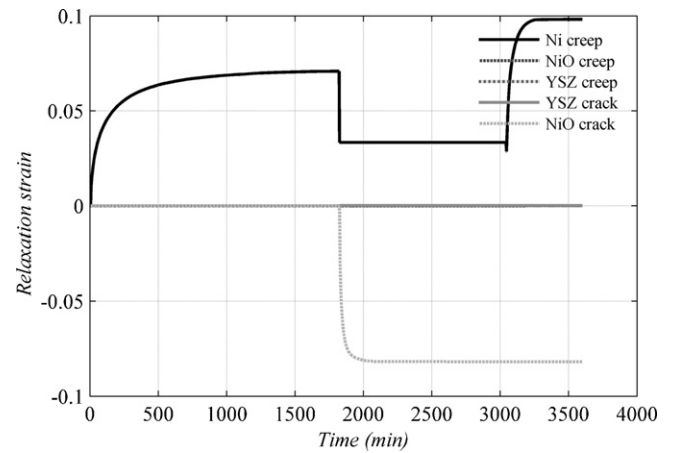**Fig. 7.** Case 1: Measured and calculated CRS during isothermal reduction and re-oxidation at 600 °C.

Fig. 8. Case 1: Different calculated deformations leading to stress relaxation during isothermal reduction and re-oxidation at 600 °C.
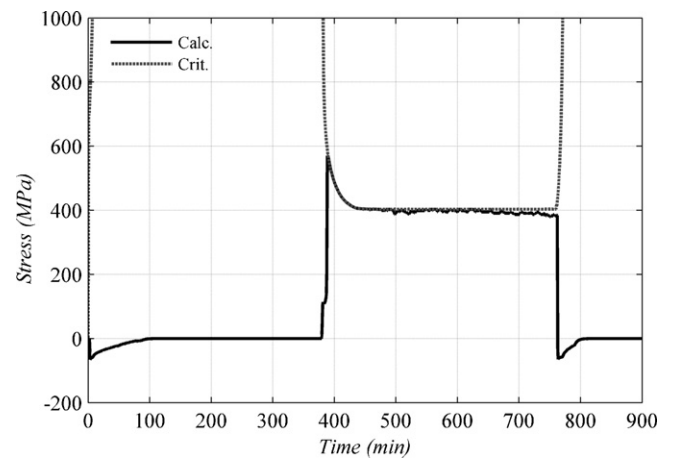

Fig. 9. Case 2: Calculated stress and the critical stress for NiO fracture during isothermal reduction and re-oxidation at 750 °C.
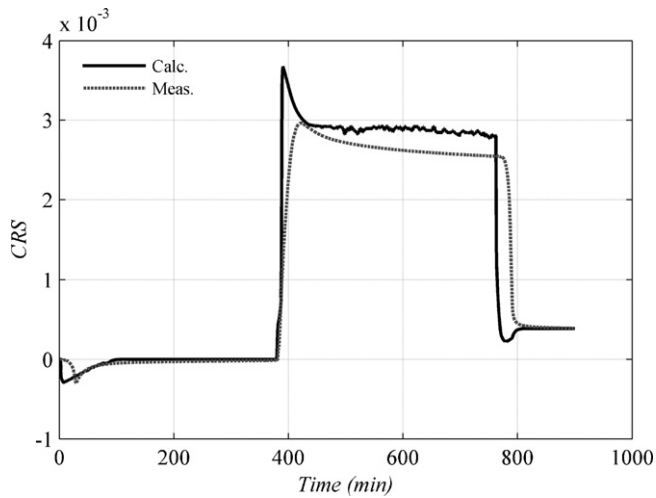
Fig. 10. Case 2: Measured and calculated CRS during isothermal reduction and re-oxidation at 750 °C.
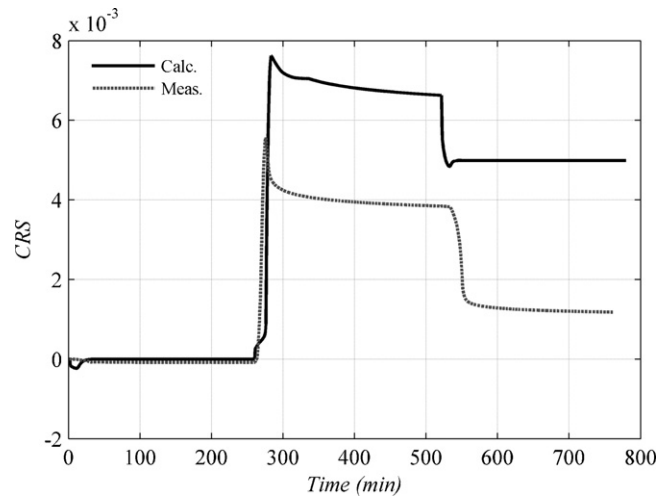

Fig. 13. Case 3: Measured and calculated CRS during isothermal reduction and re-oxidation at 850 °C. *Note*: the measured dilatometry sample buckled at $t \sim 280$ min.
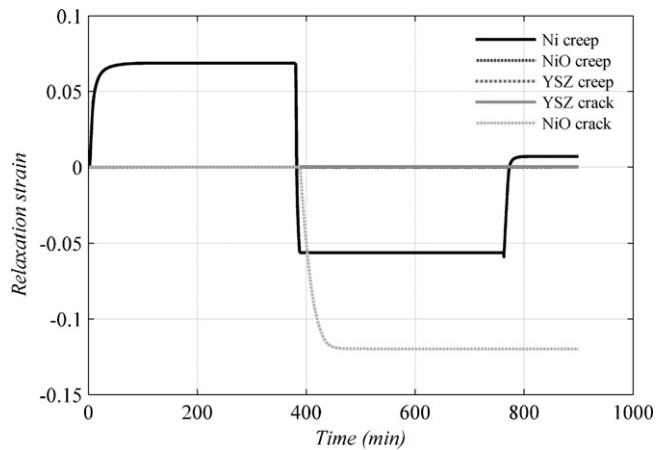

Fig. 11. Case 2: Different calculated deformations leading to stress relaxation during isothermal reduction and re-oxidation at 750 °C.
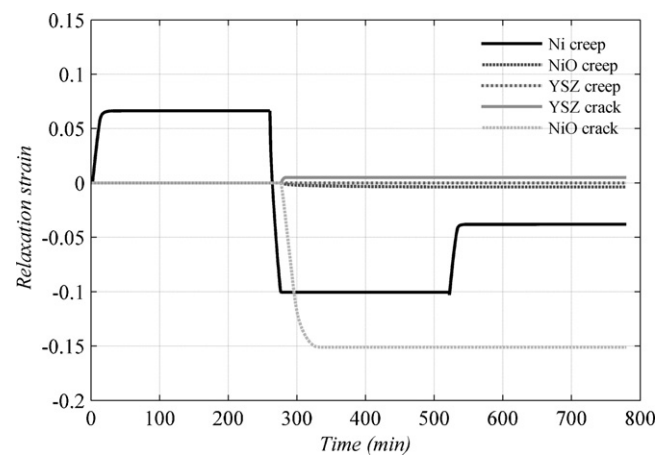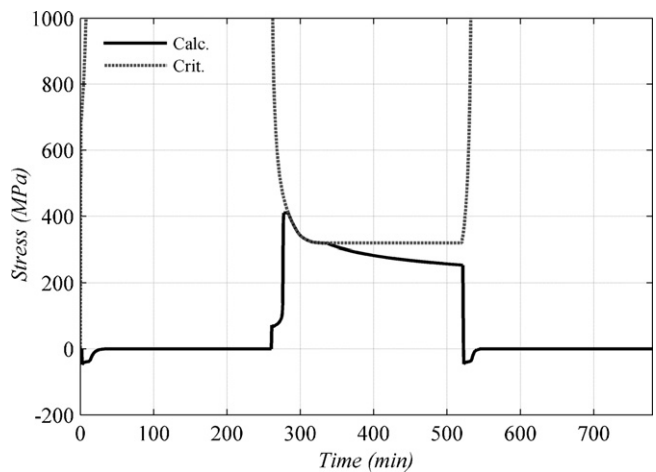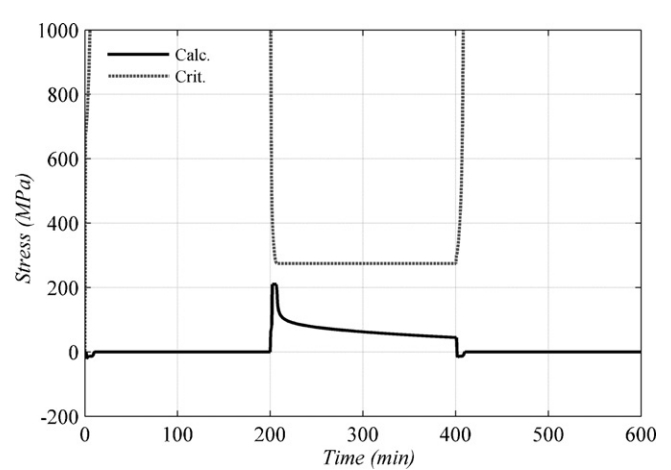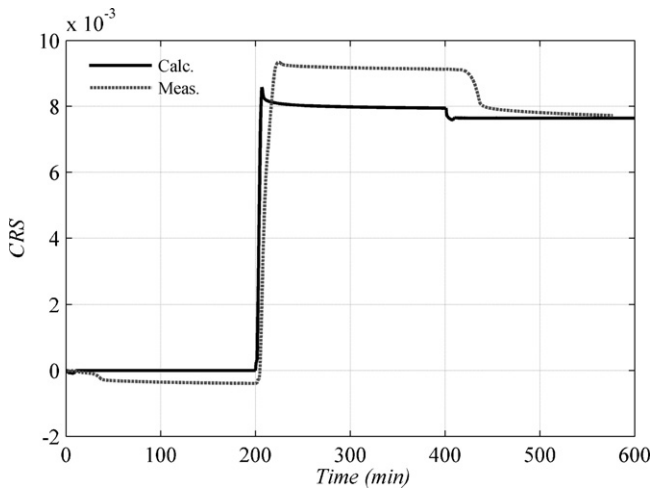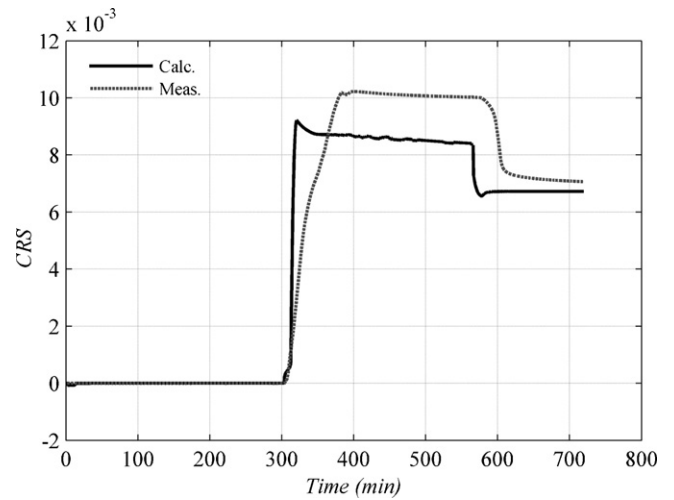

Fig. 14. Case 3: Different calculated deformations leading to stress relaxation during isothermal reduction and re-oxidation at 850 °C.

Fig. 12. Case 3: Calculated stress and the critical stress for NiO fracture during isothermal reduction and re-oxidation at 850 °C.

Fig. 15. Case 4: Calculated stress and the critical stress for NiO fracture during isothermal reduction and re-oxidation at 1000 °C.

Fig. 16. Case 4: Measured and calculated CRS during isothermal reduction and re-oxidation at 1000 °C.

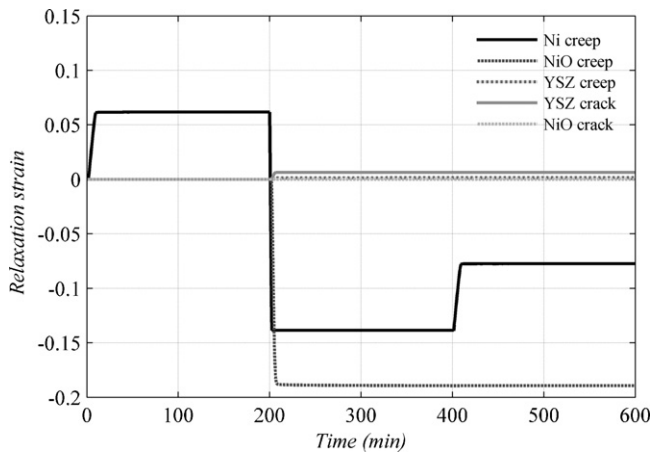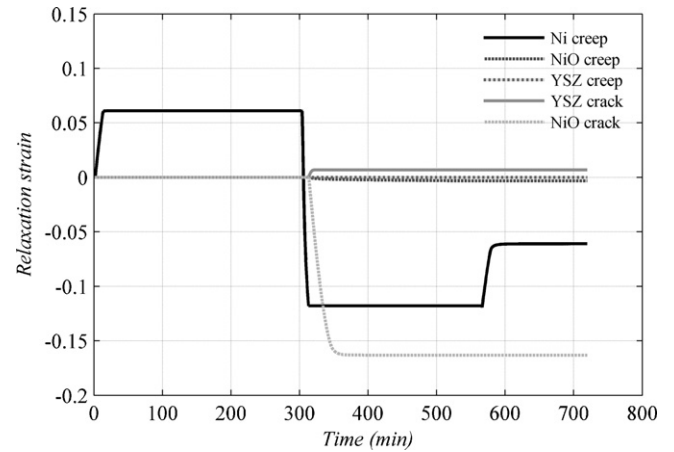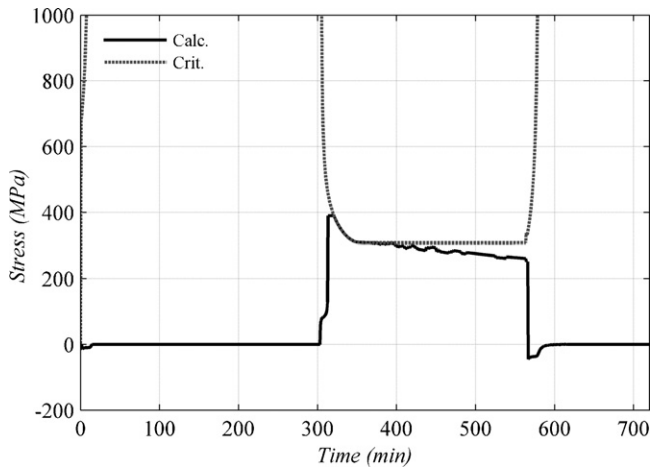**Fig. 19.** Case 5: Measured and calculated CRS during isothermal reduction at 1000 °C and re-oxidation at 850 °C.

Fig. 17. Case 4: Different calculated deformations leading to stress relaxation during isothermal reduction and re-oxidation at 1000 °C.

Fig. 20. Case 5: Different calculated deformations leading to stress relaxation during isothermal reduction at 1000 °C and re-oxidation at 850 °C.

Fig. 18. Case 5: Calculated stress and the critical stress for NiO fracture during isothermal reduction at 1000 °C and re-oxidation at 850 °C.
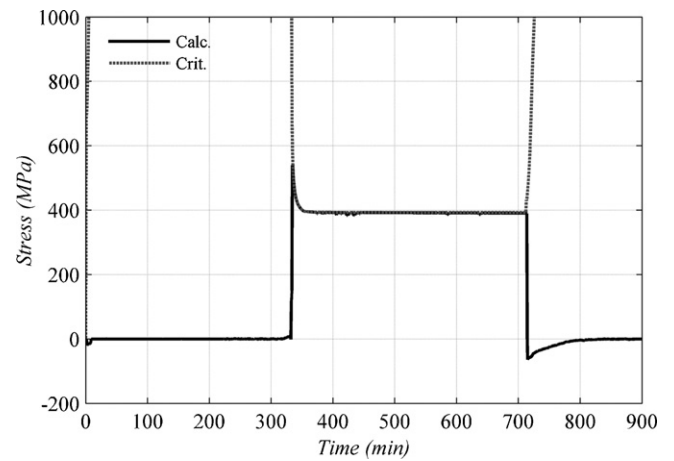

Fig. 21. Case 6: Calculated stress and the critical stress for NiO fracture during isothermal reduction at 1000 °C and re-oxidation at 750 °C.
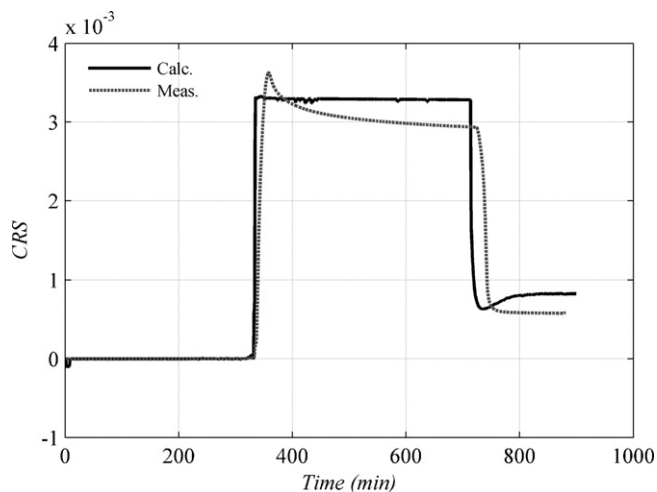
Fig. 22. Case 6: Measured and calculated CRS during isothermal reduction at 1000 °C and re-oxidation at 750 °C.

5. Discussion

Results on the dimensional behaviour of typical isotropic Ni–YSZ microcomposites for SOFC have been reported earlier and the general observations upon isothermal reduction and subsequent re-oxidation, using different combinations of reduction and re-oxidation temperatures, can be summarised as follows [5,14]:

1. On the first reduction at low temperatures (600 °C), an initial contraction is observed, followed by a recovery towards the initial dimension. When elevating the reduction temperature to 750 °C, the contraction is still observed but smaller. At even higher temperatures, the initial contraction first disappears at 850 °C and at 1000 °C a small permanent shrinkage is perceived.
2. When reducing the NiO–YSZ at two temperatures and then re-oxidising the reduced cermets at the lower of those temperatures, the redox strain of the sample reduced at the higher temperature was slightly more when the re-oxidation temperature exceeded about 800 °C. A high initial reduction temperature leads to rapid Ni particle growth through sintering. The growth of the Ni particles leads to a negative impact on the redox stability. When the temperature of re-oxidation was about 750 °C or lower, such a difference depending on the reduction conditions was not perceived, however.
3. When similar samples were identically reduced at a high temperature (1000 °C) and subsequently re-oxidised in the tem-
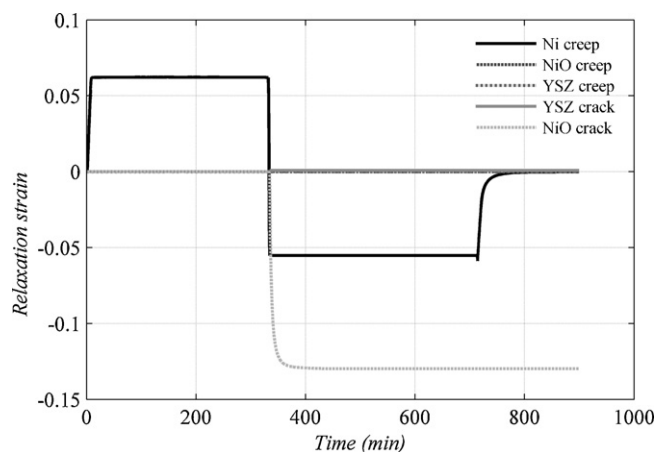

Fig. 23. Case 6: Different calculated deformations leading to stress relaxation during isothermal reduction at 1000 °C and re-oxidation at 750 °C.
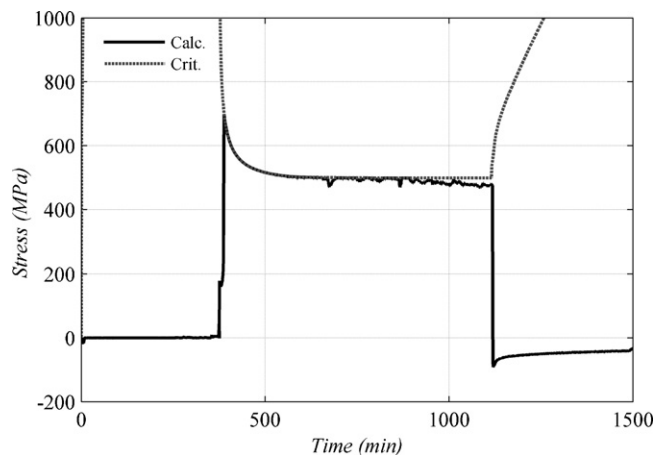

Fig. 24. Case 7: Calculated stress and the critical stress for NiO fracture during isothermal reduction at 1000 °C and re-oxidation at 600 °C.
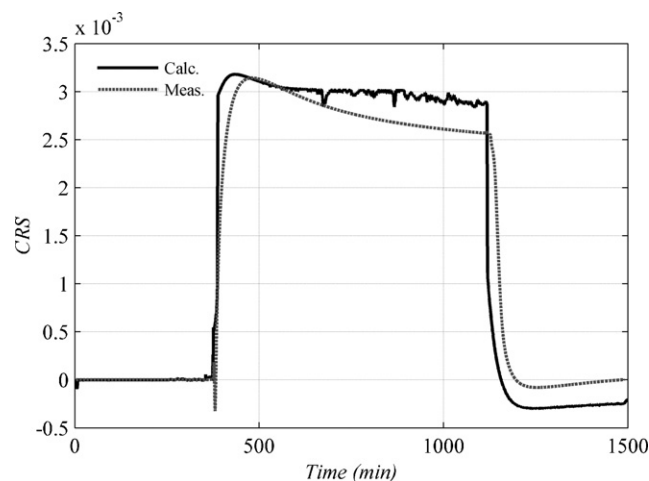

Fig. 25. Case 7: Measured and calculated CRS during isothermal reduction at 1000 °C and re-oxidation at 600 °C.

perature range 600–1000 °C, the dimensional behaviour divided into two domains. At temperatures of approximately 750 °C and below, the redox strain is significantly less than in cases where the re-oxidation temperature is high (850–1000 °C). With the initial Ni–YSZ microstructure being the same, the differences in the behaviour arise from the oxidation process and the resulting NiO microstructure, as well as the mechanical properties of the oxidising phase and the YSZ.
4. The reversibility of the redox strain in a complete redox cycle (reduced state–re-oxidation–re-reduction) is a measure of the type of the deformation processes occurring in the YSZ backbone due to the redox cycling. The reversible deformation processes are the elastic and anelastic strains due to the redox stress, whereas the irreversible processes comprise plastic deformation (creep) and micro/macrocracking. Note that in the present treatment, the bulk dimensions of the composite are given by the YSZ deformation and even with that being reversible, an irreversible creep deformation or microcracking of the Ni/NiO phase is allowed to occur.

The above four observations are reproduced by the current model and the parameter selection with a relatively good agreement. First, the model predicts the initial contraction and recovery towards the initial length on low temperature reduction (cases 1 and 2). The calculated stress levels (compressive stress calculated
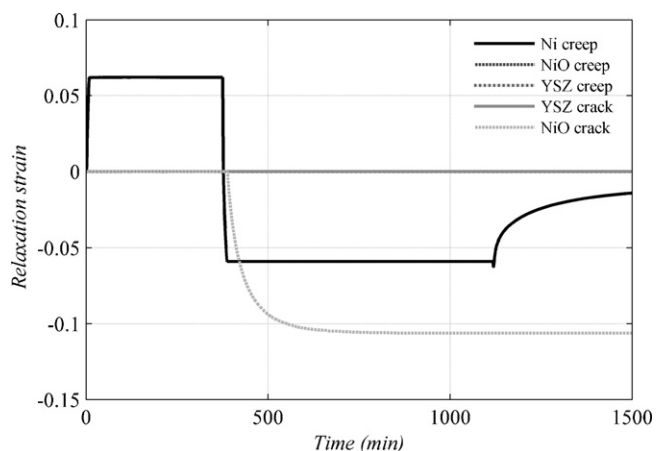
Fig. 26. Case 7: Different calculated deformations leading to stress relaxation during isothermal reduction at 1000 °C and re-oxidation at 600 °C.

in the YSZ, tensile in the Ni/NiO phase) during the reduction in case 1 and 2 are in the order of 50–100 MPa. The simulated relaxation of this stress takes place almost exclusively as creep in the Ni phase. The observed contraction results in as a combination of the kinetics of reduction and the mechanical properties of the Ni/NiO phase. With elevating reduction temperature in cases 3 and 4, creep relaxation in Ni becomes faster and subsequently the initial contraction diminishes.

Second, the difference in redox strain when varying the initial reduction temperature and subsequently re-oxidising at a same temperature is about 0.05–0.1% or less in all temperature combinations, comparing case 1 to case 7, case 2 to case 6 and case 4 to case 5. In all three comparisons the simulated CRS are quite similar. The differences in the CRS vs. time depend on slightly different reaction kinetics in each case from the TGA measurements. This affects, through the selected model parameters, mostly the active time window for Ni creep relaxation. In the initial stages of the re-oxidation, stress relaxation by Ni creep is the dominant relaxation mechanism. Soon after the effective DoO approaches unity, however, the stress increases up to the critical stress in NiO and pseudoplasticity relaxation in NiO starts. It is important to emphasise that it turned out to be impossible to simulate the experimentally observed dimensional behaviour without taking into account stress relaxation by pseudoplasticity in the NiO phase; diffusional creep rates in NiO are insufficient to relax the chemical stresses produced except for re-oxidation at 1000 °C. At 1000 °C (case 4) the diffusional creep of NiO was high enough so that the stress did not reach the critical stress for scale cracking. The simulated expansion during the re-oxidation depends on the nonelastic relaxation strain in the Ni/NiO phase. Neither the creep properties of the partially oxidised Ni/NiO phase nor the critical strain and strain rate leading to pseudoplasticity are accurately known.

The third general observation pertaining to the re-oxidation phase is well reproduced by the model. The calculated stresses during the re-oxidation in cases 5–7 are about 300, 400 and 500 MPa, respectively, with the initial stress peak reaching in all cases 100–200 MPa higher. The difference between the simulated behaviour on high temperature 850–1000 °C (cases 4 and 5) and the low temperature 600–750 °C (cases 6 and 7) re-oxidation is that in the former two, nonelastic strains develop in the YSZ phase. In case 4 the nonelastic strain consists of both YSZ creep (mainly GBS) and cracking, whereas in case 5 it comes to a large extent from YSZ cracking. These nonelastic YSZ strains, while relaxing part of the effective chemical strain, also lead to the strain irreversibility of the redox cycle; upon re-reduction of the composite it does not return to the initial dimension but

instead a permanent elongation results in. This result from the simulations is largely in line with the observations from the measurements.

It is good to bear in mind, however, that the calculated nonelastic stain in YSZ due to cracking is closely related to the parameter value used for the TZP strength—a fitted parameter in these simulations. In the same way, the critical stress for relaxation in NiO by pseudoplasticity is directly dependent on the value used for NiO fracture toughness K_{IC} (and the critical flaw size). By a selection of TZP strength the critical strain in NiO, basically any redox strain level could be simulated. This said, on the other hand, if and when the rest of the literature-based model parameters are relatively well in place in the calculation and a constant value of K_{IC}(NiO) is used, we have 'backwards' modelled a trend in the strength of TZP versus temperature. This type of result would imply that the mechanical characteristics of tetragonal zirconia do play a role in the structural durability of the composites towards lower temperatures.

6. Conclusions

A continuum mechanics model was developed to simulate the dimensional behaviour of NiO/Ni–YSZ composites during reduction–re-oxidation cycles at high temperature. The model starts from the chemical strains arising from the phase change Ni ↔ NiO and takes into account different nonelastic strains to relax the stresses. Creep models for Ni, NiO and YSZ were implemented, as well as simple semi-empirical models for pseudoplasticity of NiO and cracking of YSZ. Several semi-empirical correlations were incorporated to account for different known subprocesses.

Seven redox dilatometry experiments were simulated using experimental reduction–oxidation kinetics information from similar TGA experiments. The experiments comprised four different reduction temperatures isothermally followed by re-oxidations, and three cases where the initial reduction was carried out at a high temperature and the re-oxidation temperature was lower. Generally, the continuum model reproduces the dimensional behaviour of the composites with a fairly good agreement.

The main stress relaxation processes in each stage of redox cycling were identified. During the initial reduction, creep rates in the Ni/NiO phase determine whether or not contraction occurs during the initial stage. On re-oxidation, the early stages of the oxidation process metallic Ni can still creep to relax the stress, but later in the re-oxidation the implementation of stress relaxation by pseudoplasticity and microcracking in the NiO phase becomes instrumental in reaching any kind of fit to the measured data.

The increase in the redox strain and damage observed upon re-oxidation at high temperatures was well reproduced by the model. This increase in redox strain resulted from nonelastic strains in the YSZ phase. At 1000 °C the strain came from YSZ creep (GBS) and microcracking of the YSZ, and at 850 °C mainly from fractures in the YSZ backbone. The loss of strain reversibility on re-reduction of the re-oxidised composite was in the simulations a direct result of the nonelastic strains produced in the YSZ phase.

References

[1] W.Z. Zhu, S.C. Deevi, Mater. Sci. Eng. A362 (2003) 228–239.
[2] D. Sarantaridis, A. Atkinson, Fuel Cells 7 (2007) 246–258.
[3] D. Simwonis, F. Tietz, D. Stöver, Solid State Ionics 132 (2000) 241–251.
[4] J. Sehested, J.A.P. Gelten, I.N. Remediakis, H. Bengaard, J.K. Nørskov, J. Catal. 223 (2004) 432–443.
[5] M. Pihlatie, A. Kaiser, P.H. Larsen, M. Mogensen, J. Electrochem. Soc. 156 (2009) B322–B329.
[6] M. Pihlatie, T. Ramos, A. Kaiser, J. Power Sources 193 (2009) 322–330.
[7] P. Kofstad, High Temperature Corrosion, Elsevier Applied Science, London, 1988.
[8] A. Atkinson, Rev. Mod. Phys. 57 (1985) 437–470.
[9] R. Haugsrud, Corros. Sci. 45 (2003) 211–235.
[10] H.V. Atkinson, Oxidat. Met. 28 (1987) 353–389.
[11] T. Klemensø, PhD Thesis, Technical University of Denmark, 2005.
[12] D. Sarantaridis, A. Atkinson, in: Proceedings of the 7th European SOFC Forum, Lucerne, Switzerland, Paper P0728, 2006.
[13] J. Laurencin, G. Delette, F. Lefebvre-Joud, M. Dupeux, J. Eur. Ceram. Soc. 28 (2008) 1857–1869.
[14] M. Pihlatie, A. Kaiser, M. Mogensen, Solid State Ionics 180 (2009) 1100–1112.
[15] A.S. Nowick, B.S. Berry, Anelastic Relaxation in Crystalline Solids, Academic Press, New York, 1972.
[16] R.S. Lakes, Viscoelastic Solids, CRC Press, 1998.
[17] M. Matsuzawa, E. Fujimagari, S. Horibe, Mater. Sci. Eng. A314 (2001) 105–109.
[18] M. Matsuzawa, S. Horibe, Mater. Sci. Eng. A 346 (2003) 75–82.
[19] M. Matsuzawa, F. Sato, S. Horibe, J. Mater. Sci. 36 (2001) 2491–2497.
[20] M. Matsuzawa, F. Sato, S. Horibe, ISIJ Int. 43 (2003) 555–563.
[21] G.E. Dieter, Mechanical Metallurgy SI Metric Ed., McGraw-Hill, London, 1988.
[22] W.R. Cannon, T.G. Langdon, J. Mater. Sci. 18 (1983) 1–50.
[23] W.R. Cannon, T.G. Langdon, J. Mater. Sci. 23 (1988) 1–20.
[24] T.G. Langdon, J. Mater. Sci. 41 (2006) 597–609.
[25] C. Herring, J. Appl. Phys. 21 (1950) 437–445.
[26] R.L. Coble, J. Appl. Phys. 34 (1963) 1679–1682.
[27] A.H. Chokshi, Scripta Mater. 48 (2003) 791–796.
[28] M. Jiménez-Melendo, A. Domínguez-Rodríguez, Acta Mater. 48 (2000) 3201–3210.
[29] A. Domínguez-Rodríguez, D. Gómez-García, M. Castillo-Rodríguez, J. Eur. Ceram. Soc. 28 (2008) 571–575.
[30] M. Jiménez-Melendo, A. Domínguez-Rodríguez, J. Castaing, R. Marquez, Scripta Metallurgica 20 (1986) 739–742.
[31] M. Jiménez-Melendo, A. Domínguez-Rodríguez, R. Marquez, Philos. Mag. A 56 (1987) 767–781.
[32] H.J. Frost, M.F. Ashby, Deformation-Mechanism Maps, The Plasticity and Creep of Metals and Ceramics, 1st edition, Pergamon Pr., 1982. http://engineering.dartmouth.edu/defmech/.
[33] M. Pihlatie, A. Kaiser, M. Mogensen, J. Eur. Ceram. Soc. 29 (2009) 1657–1664.
[34] I.A. Menzies, K.N. Strafford, J. Mater. Sci. 2 (1967) 358–364.
[35] R. Farraro, R.B. McLellan, Metall. Trans. A 8A (1977) 1563–1565.
[36] A. Atkinson, A. Selcuk, Solid State Ionics 134 (2000) 59–66.
[37] A. Faes, H.L. Frandsen, M. Pihlatie, A. Kaiser, D.R. Goldstein, Journal of Fuel Cell Science and Technology, in press.
[38] L.S. Pan, N. Imai, S. Horibe, Mater. Sci. Eng. A230 (1997) 155–160.
[39] R. Danzer, P. Supancic, J. Pascual, T. Lube, Eng. Fract. Mech. 74 (2007) 2919–2932.
[40] T. Klemensø, M. Mogensen, J. Am. Ceram. Soc. 90 (11) (2007) 3582–3588.
[41] R. Danzer, J. Eur. Ceram. Soc. 26 (2006) 3043–3049.
[42] I. Küppenbender, M. Schütze, Oxidat. Met. 42 (1994) 109–143.
[43] M. Schütze, Oxidat. Met. 25 (1986) 409–421.
[44] P. Hancock, J.R. Nicholls, Mater. Sci. Technol. 4 (1988) 398–406.
[45] M. Radovic, E. Lara-Curzio, Acta Mater. 52 (2004) 5747–5756.
[46] C. Bruns, M. Schütze, Oxidat. Met. 55 (2001) 35–67.
[47] A.G. Evans, D. Rajdev, D.L. Douglass, Oxidat. Met. 4 (1972) 151–170.
[48] H. Yokokawa, H. Tu, B. Iwanschitz, A. Mai, J. Power Sources 182 (2008) 400–412.
[49] J. Sehested, J.A.P. Gelten, S. Helveg, Appl. Catal. A: Gen. 309 (2006) 237–246.
[50] T. Klemensø, C. Chung, P.H. Larsen, M. Mogensen, J. Electrochem. Soc. 152 (2005) A2186–A2192.
[51] R. Vassen, D. Simwonis, D. Stöver, J. Mater. Sci. 36 (2001) 147–151.
[52] A.W. Harris, J.S. Brown, A. Atkinson, Corros. Sci. 34 (1993) 1017–1033.
[53] A. Morales-Rodríguez, A. Bravo-León, A. Domínguez-Rodríguez, S. López-Esteban, J.S. Moya, M. Jiménez-Melendo, J. Eur. Ceram. Soc. 23 (2003) 2849–2856.
[54] A. Morales-Rodríguez, A. Bravo-León, G. Richter, M. Rühle, A. Domínguez-Rodríguez, M. Jiménez-Melendo, Scripta Mater. 54 (2006) 2087–2090.